Chapter 9
Experimental and Theoretical Issues of Nanoplasmonics in Medicine

Daniel A. Travo, Ruby Huang, Taiwang Cheng, Chitra Rangan, Erden Ertorer, and Silvia Mittler

9.1 Introduction

Biosensors are comprised of two components: a biomolecule that binds highly specifically to an analyte and a transducer that converts the biomolecular recognition to signal. Gold nanoparticles (GNPs) exhibit unique optical properties, which make them suitable for bio-sensing applications. The high affinity of gold to thiol (–SH) groups (which is strong but reversible) allows functional group attachments to biomolecules. The attachment of any organic material to nanogold produces a large change in its optical scattering properties. The combination of these two properties has lead to the development of GNP biosensors.

Recently, GNPs have found tremendous use in biological assays, detection, labeling, and sensing. GNP-based methods have been applied to screening for hepatitis A, hepatitis B, HIV, Ebola, smallpox,

D.A. Travo • R. Huang • T. Cheng • C. Rangan (✉)
Department of Physics, University of Windsor, Windsor, ON, Canada
e-mail: rangan@uwindsor.ca

E. Ertorer
Biomedical Engineering Program, Western University, London, ON, Canada

Department of Physics and Astronomy, Western University, London, ON, Canada

S. Mittler (✉)
Department of Physics and Astronomy, Western University, London, ON, Canada
e-mail: smittler@uwo.ca

M. Schlesinger (ed.), *Applications of Electrochemistry in Medicine*, Modern Aspects of Electrochemistry 56, DOI 10.1007/978-1-4614-6148-7_9,

and anthrax without any false negatives or false positives [8]. A GNP's optical spectrum is a probe of the localized surface plasmon resonance (LSPR) phenomenon, a collective electronic excitation that is localized in spatial extent due to the small size of the nanoparticle compared to the wavelength. The optical resonance frequency of the GNPs is a function of size, shape, interparticle distance and surrounding medium [18, 24].

In modern sensing applications, nanoparticles are immobilized on a surface in order to present the maximum detection surface to the analyte. A surface platform also allows for multiplexing—a device that tests multiple analytes in the same sample, which opens doors to the possibility of screening multiple diseases simultaneously. This configuration is well known to researchers in the surface science community as surface quantum dots or supported thin-film islands.

Surface immobilized GNP platforms provide significant advantages over 3D or colloidal gold sensor platforms. In spite of the simplicity of production of colloidal gold, solution-based GNPs need a stabilizing agent to prevent aggregation. This is achieved by adding a citrate layer or a polymer coating to create a core-shell structure [10]. This introduction of additional surface chemistry complicates further functionalization. The same issues are problematic for substrate-immobilized colloidal GNP systems. Colloidal gold requires additional handling considerations for lab-on-a-chip applications. In contrast, surface immobilized particles do not need stabilization against aggregation. Their bare surface allows easy functionalization using thiol chemistry.

This chapter documents the experimental issues concerning the fabrication of surfaces upon which GNPs are immobilized, and the theoretical issues concerning the modeling of such structures. In particular, the challenges and advantages of Organometallic Chemical Vapor Deposition (OMCVD) are presented. We also compare and contrast various theoretical approaches of modeling the optical properties of this system.

9.2 Fabrication of Surface Immobilized GNP Platforms

Conventional fabrication methods to produce surface immobilized nanoparticles such as Focused Ion Beam (FIB) or Electron Beam Lithography not only require high investment for the setups, their

operating costs are high too and they suffer from low speed and small coverage area. For research and development purposes these disadvantages can be neglected; however, for industrial or clinical applications where mass production is required, simple, cost-effective, and fast methods are required.

OMCVD is a well-known method to create metallic thin films on substrate surfaces and can also be used for fabricating surface immobilized GNPs. OMCVD grown NP are randomly distributed and chemically attached to the substrate [14, 20, 44]. Although it is a statistical process, it yields narrow GNP size distributions which makes the surfaces suitable for biosensor applications. The hemispherical shape of the GNPs provides more stability [4]. The fabrication process is simple and inexpensive: it involves simple beaker chemistry and is performed at low temperatures (~65 °C). In this section, we will discuss OMCVD grown GNPs for plasmonic sensor applications with all the aspects; from preparation of the substrate surface for OMCVD process to biosensor application.

9.2.1 Substrate Selection

There are two main aspects in substrate selection: chemical and optical properties. Chemical composition and surface chemistry have a huge impact on the quality of the final product: particle size distribution, homogeneity, and stability of the particles. Silicon wafers are a good candidate material; however, transmission-based LSPR sensors require transparency at the range of the LSPR wavelength. This wavelength depends on the size of the GNPs and corresponds typically in the visible to near infrared region of the spectrum. On the other hand, if the sensor is based on an optical waveguide in an optical lab-on-a-chip, the substrate should be suitable for waveguide fabrication procedures, e.g., ion exchange. BK7 (Schott, Germany) is a high quality glass, exhibiting more than 90% transmission between 350 nm and 2,500 nm [37]. Ion exchange and surface functionalization properties are well studied [4, 40, 42].

9.2.2 *Surface Preparation with Silane Self-Assembled Monolayers*

In contrary to physical vapor deposition (PVD), CVD and OMCVD are selective processes [14]. Selectivity is provided by the surface chemistry; chemical interaction between the substrate and the material to be deposited play a major role. Substrate surfaces need to be adapted and therefore modified to provide chemisorption of the target atoms. The stability of the NPs depends on the chemical with which they bind to the substrate surface. Quality of the surface functionalization is critical. For plasmonic sensor applications, physisorbed particles would be able to move on the surface due to a lack of proper bonding and will aggregate. This aggregation is irreversible and provides false sensor signal due to this undesired clustering effect (see Fig. 9.5b, c). Furthermore, losing NPs during the sensing process due to detachment will decrease the signal and the signal-to-noise ratio. Therefore the substrate surface must be functionalized in such a way that it is ensured to obtain particles that are chemically attached to the surface. Gold has a strong affinity to thiols [15] and amines [6]. Therefore surface functionalization can be carried out employing thiol or amine groups in self-assembly processes. Mercapto-propyl-trimethoxy-silane (MPTMS) is a compound to silanize glass surfaces for a functionalization with thiol (mercapto) groups [41] (Fig. 9.1e). Hexamethyldisilazane (HMDS) is commonly used for adhesion promoter of photoresists for lithography applications [31], with an amine head group (Fig. 9.1f). Surface functionalization to promote GNP growth via OMCVD can be done by either of these methods.

Figure 9.1 illustrates the steps towards silanized surfaces and the necessary silanes. For the silanization the cleaned glass surface (Fig. 9.1a) should be oxidized since the silane groups of MPTMS and HMDS attach to oxidized surfaces (–OH) to form a silane network on the substrate (Fig. 9.1c, d). A piranha solution procedure is a common method to oxidize the substrate surfaces. Two hours of immersion in a freshly prepared 3:1 sulfuric acid:hydrogen peroxide solution forms hydroxyl groups on the substrate surface (Fig. 9.1b). (Caution: Piranha solution is dangerous, extremely corrosive, and violently reacts with organic materials. All safety measures should be taken to handle it). Oxygen plasma treatment is another way to oxidize glass substrate surfaces. Twenty minutes of treatment cleans

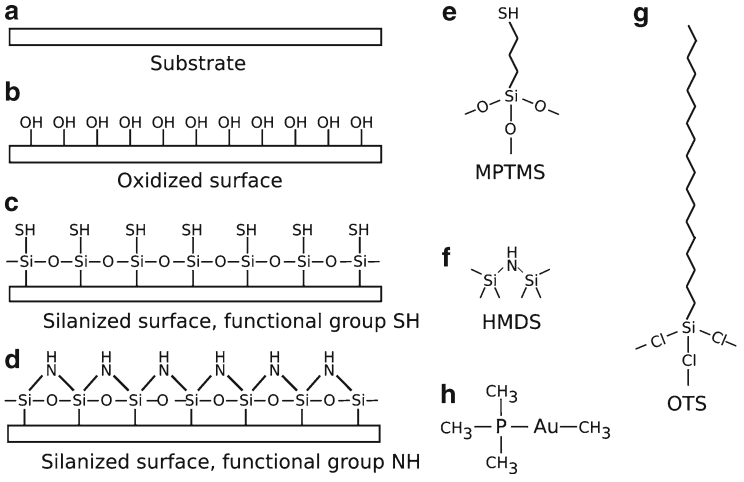

Fig. 9.1 (**a**) BK7 substrate, (**b**) oxidized surface, (**c**) thiol functionalized surface, (**d**) amine functionalized surface, (**e**) MPTMS, (**f**) HMDS, (**g**) OTS, (**h**) gold precursor ($[(CH_3)_3P]AuCH_3$)

the surface and functionalized the surface with hydroxyl groups. Surface modification due to the piranha or plasma treatment can be verified by contact angle measurements. After the oxidation treatment the glass surface turns hydrophilic and the contact angle of water drops below 4°.

After piranha treatment, substrates should be rinsed with abundant amounts of deionized water. Nitrogen-dried samples are placed in a vacuum oven at 95 °C for dehydration for an hour. The removing of possible moisture on the substrates is necessary as moisture causes uncontrolled polymerization of MPTMS and reduces the quality of self-assembled monolayer. For MPTMS silanization samples are immersed in 1:100 (V/V) MPTMS and ethanol (anhydrous) solution under argon environment in a glove box overnight. After rinsing and drying, baking in a vacuum oven at 95 °C for 20 min establishes the silane network on the surface.

HMDS functionalization is carried out in an oven (YES-3TA HDMS Oven, Yield Engineering, CA, USA). Because of the automatization of the HDMS process, more stable and reproducible samples can be achieved with the HMDS and oxygen plasma treatment combination.

9.3 OMCVD Process

OMCVD is a common method to deposit metallic thin film layers. If the interaction energy between the deposited metal atoms is higher than the metal–substrate interaction energy, island growth occurs [31]. This principle can be implemented to produce metallic NP instead of thin films [14]. Conventional CVD setups are usually dynamic which means they have a mass transport system to carry the precursor. The precursor is the chemical compound which contains the metal to be deposited. Previous studies show that for GNPs growth dynamic reactors do not show any significant advantages over static ones [3]. Additionally, it requires complex modules such as a gas flow handling system and consumes higher amounts of precursor. The static setup is simple; the reactor consists only of a vacuum chamber with a valve. The volatile precursor and the samples are placed on the bottom of the reactor (Fig. 9.2). Heating the evacuated reactor evaporates the precursor and heats the samples for the OMCVD process.

GNPs could attach to the reactor surface. That means less gold for the substrates. Silanization of the chamber with octadecyltrichlorosi-

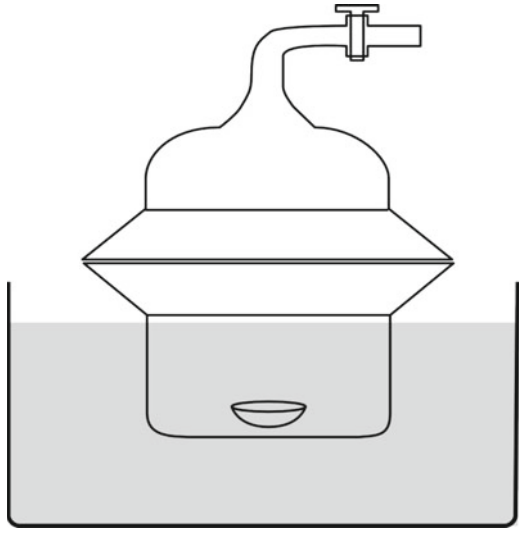

Fig. 9.2 Reactor in a water bath. A watch glass containing the precursor is placed on the reactor bottom with the samples

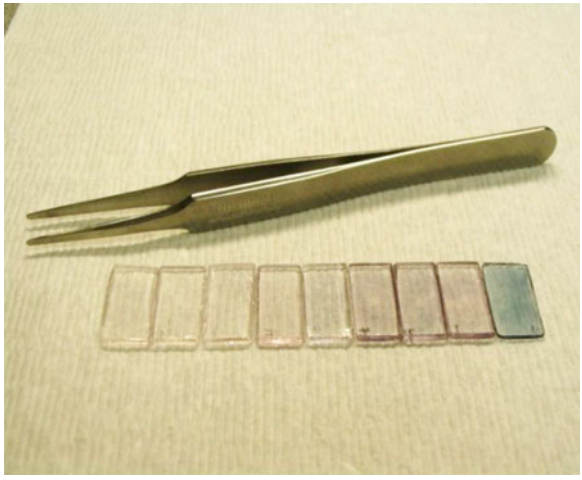

Fig. 9.3 Samples with OMCVD grown gold nanoparticles

lane (OTS) would avoid physisorption of the GNPs on the reactor chamber.

Trimethylphosphinegoldmethyl ($[(CH_3)_3P]AuCH_3$) is an organometallic precursor (Fig. 9.1h) which is known to deliver pure thin films of gold at relatively low temperatures [16]. Working at low temperature makes this precursor compatible with organic compounds such as self-assembled monolayers of MPTMS or HMDS. $[(CH_3)_3P]AuCH_3$ has a very small vapor pressure and evaporates at temperatures as low as room temperature. When the precursor evaporates and touches the functionalized surface, the precursor molecule breaks up and releases the gold atom from the molecule. The gold atom attaches to the functionalized substrate surface or another gold atom previously deposited forming GNPs. The phosphine group and the methyl stay in the vapor phase.

Using an oven as a heat source for the reactor increases the evaporation speed of the precursor. However, this method yields high inhomogeneities; the sample to sample differences are large and the GNP distribution along an individual sample is inhomogeneous. This nonuniformity can be seen qualitatively by the naked eye due to the color the GNPs produce (Fig. 9.3), but can also be detected quantitatively by UV-Vis absorption spectroscopy (Fig. 9.4a). Since there is no external gas flow into the chamber,

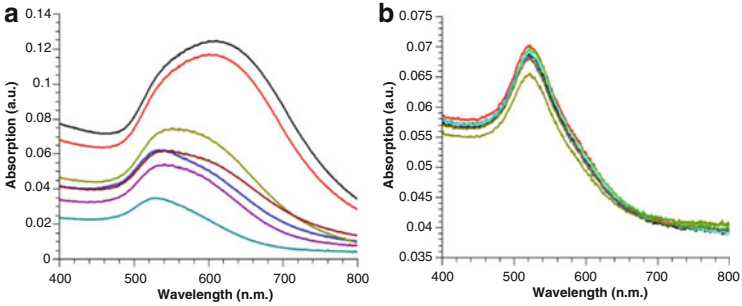

Fig. 9.4 Absorption spectra of two different GNP batches; GNP growth performed (**a**) in an uneven bottom reactor and an oven as the heating source, and (**b**) in a flat bottom reactor in a water bath

mass transport is provided by internal convection. Heating the entire chamber does not create a uniform convection. Placing the chamber partially in a water bath provides a uniform temperature gradient increasing the homogeneity along the sample surface as well as between the samples and increases reproducibility significantly. On the other hand, surface temperature of the samples affects the reactivity, therefore reactor surface roughness adversely affect the quality of the samples and the batch. Flat bottom reactors, allowing the flat samples to have an optimum heat contact to the reactor wall, deliver the best sample homogeneity. Figure 9.4 shows UV-Vis absorption spectra of two different batches; one was oven heated in a rough bottom chamber (Fig. 9.4a) and the other one was fabricated in a flat bottom chamber in the water bath (Fig. 9.4b). OMCVD parameters were 65 °C reaction temperature and 0.050 mbar initial reactor pressure, 20 mg precursor, 17 min reaction time.

Depending on the surface chemistry and the cleanness of the inner reactor walls, undesired physisorbed GNPs are formed on the inner reactor surface. This consumption of the precursor on the reactor surfaces yields fewer nanoparticles on the samples. In order to avoid that, the reactor surface should be non-growth surfaces for the precursor. Non-growth surfaces are iter alia $–CH_3$ functionalized surfaces. These surfaces can be fabricated via silanization with OTS[26]. Following a piranha procedure, the reactor is immersed in 1:500 (v/v) OTS:toluene solution in an argon environment in a glove box overnight. After rinsing the reactor with toluene, a treatment in a vacuum oven at 95 °C for 20 min evaporates the toluene and forms the silane network on the inner surface ofthe reactor.

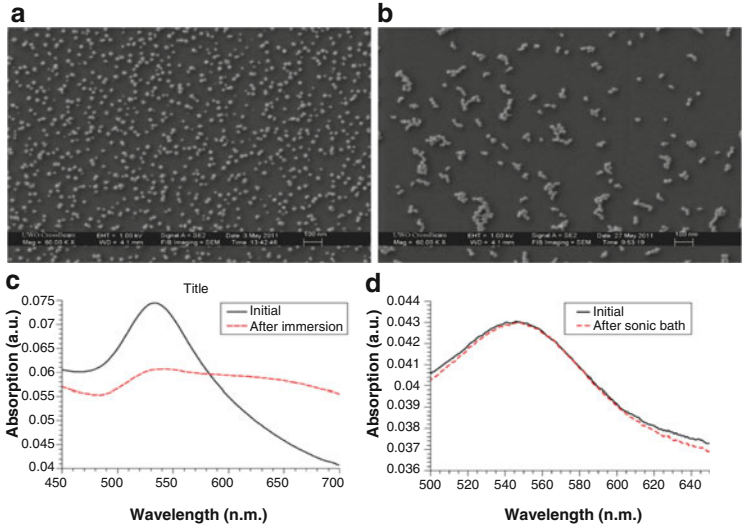

Fig. 9.5 SEM images of a sample with too many physisorbed GNPs; (**a**) before processing, (**b**) after immersing in ethanol and subsequent drying. (**c**) UV-Vis spectrum of the same sample before and after processing. (**d**) UV-Vis spectra of a sample with chemically bonded GNPs, before any treatment and after an immersion/sonication treatment

Due to the vapor process, both sides of the samples are coated. However, the bottoms of the samples (the sides that are in direct contact with the reactor wall) show less homogeneity and more physisorbed particles. This side is gently wiped with a tissue (Kimwipe) to remove the undesired GNPs. The success of all individual steps of the sample preparation procedure allows the formation of the chemical bonds between the substrate and the GNPs. If the quality of the self-assembly layer is poor, the number of physisorbed NP is high. Since they are not strongly attached to the substrate surface they can aggregate or detach from the surface while using the sample in a solution. Figure 9.5a, b shows a sample with too many physisorbed GNPs before and after immersion in ethanol and subsequent drying. Aggregation is clearly observed in the SEM image (Fig. 9.5b) as well as a decrease in the amount of GNPs. This can be observed in the UV-Vis spectra of the samples (Fig. 9.5c). Lost particles cause a decrease in the absorption signal and due to the aggregation a cross-talk shoulder appears. Therefore, the LSPR peak gets significantly wider diminishing the high sensitivity of the method. On the other

hand, the treatment of the samples in an ultrasonic bath in ethanol not only removes the physisorbed particles, but also provides a simple quality test. UV-Vis spectra of samples should not change significantly after 5 min of sonication. Figure 9.5d shows absorption spectra of a sample with chemically bonded GNPs. After 5 min of sonication in ethanol and subsequent drying the absorption spectrum does not change significantly. There is only a small amount of physisorbed particles removed.

9.3.1 Characterization

With scanning electron microscopy (SEM) the particles are imaged (Fig. 9.6a). Although glass is an insulator, the MPTMS layer in combination with the GNPs allows imaging at 1 kV gun potential. Samples with HMDS layer required a thin conductive layer for imaging with SEM, such as 1 nm of osmium.

UV-Vis absorption spectroscopy delivers some information the characteristic properties of the nanoparticles (Fig. 9.6b) since the spectra are related to the size, shape, interparticle distance, and surrounding medium of the GNPs [18, 47].

Image processing methods are employed to obtain size and interparticle distance distribution. Eight images at 100k magnification are collected from all over the sample. To yield the size information, the freeware image processing software ImageJ [1] converts the SEM image (Fig. 9.7a) into a black and white mask image (Fig. 9.7b). ImageJ then calculates the area of the particles from the mask image. Areas are converted to diameters assuming a semi-spherical particle and the diameters are displayed in histograms (Fig. 9.7c). The findmax function in ImageJ is used to find the coordinates of all particles in an image. A small program written in ImageJ calculates from these coordinates information of all particles, e.g. the center-to-center nearest neighbor distance between GNP pairs. Results are displayed in histograms as well (Fig. 9.7d).

9.3.2 Sensing

Plasmonic sensors are sensitive to the refractive index changes in their vicinity. Figure 9.8 shows a bulk refractive index experiment.

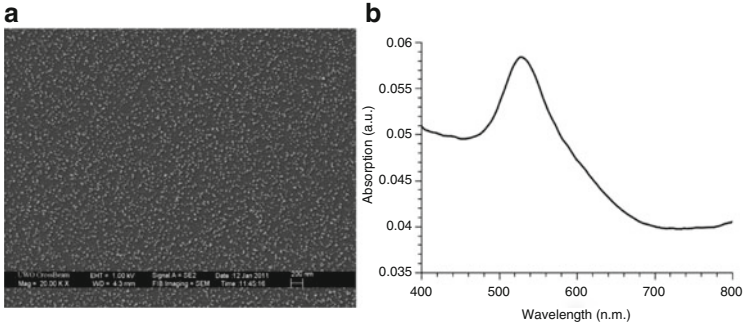

Fig. 9.6 (**a**) SEM image and (**b**) UV-Vis absorption spectrum of a sample with only chemically bonded GNPs

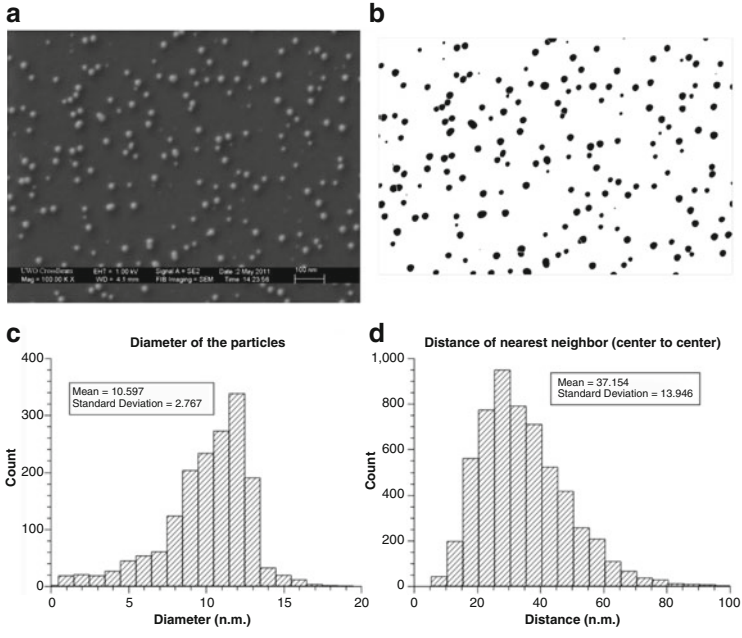

Fig. 9.7 (**a**) SEM image and (**b**) *black* and *white* mask image of a sample. (**c**) Size and (**d**) center-to-center nearest neighbor interparticle distance histograms of the nanoparticles in the sample

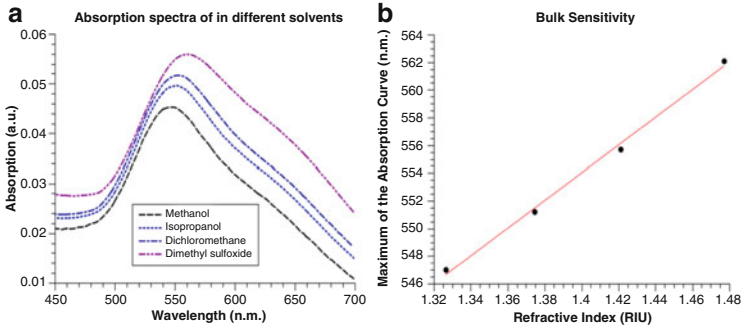

Fig. 9.8 (**a**) Absorption spectra of a sample immersed in various solvents with systematically increasing refractive index. (**b**) Wavelength of the maximum in the absorption curve versus the refractive index of the solvents

Immersing the sample in solutions with different refractive indices changes the LSPR frequency (Fig. 9.8a). An increasing refractive index causes a red shift in the maximum of the absorption curve (Fig. 9.8a). If the average interparticle distance is low enough for optical cross-talk, an increasing refractive index also increases the efficiency of the cross-talk. The cross-talk peak appears as a shoulder in the absorption spectra [35, 36].

9.3.3 Protein Sensing

Bulk sensing gives an idea about the sensing capabilities of the sensor platform. However, surface sensing would be more realistic for the practical applications. Biosensors are comprised of two components: a biomolecule that exhibits highly specific binding to an analyte (recognition), and a transducer that converts the biomolecular recognition to signal. The high affinity of gold to thiol (–SH) groups (which is strong but reversible) allows functional group attachments to biomolecules. The attachment of any organic material to nanogold produces a large change in its optical scattering properties. The combination of these two has lead to the development of GNP biosensors.

Biotin–streptavidin binding is one of the most common ways to evaluate protein sensing capabilities of a sensors. Streptavidin is a large protein (50,000 Dalton) which has four binding sites for biotin.

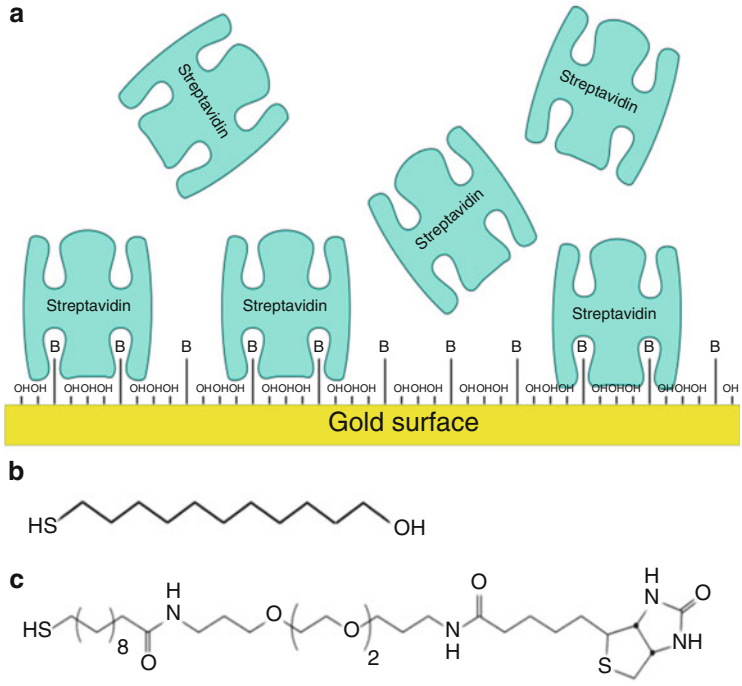

Fig. 9.9 (**a**) Illustration of streptavidin binding. (**b**) –OH terminated thiol and (**c**) biotinilated thiol

Biotin has the strongest biologically known affinity (K_a $10^{13}\,M^{-1}$). Figure 9.9 shows the binding mechanism schematically. Streptavidin binds to a properly biotinilated surface selectively and with this above-mentioned ultra-high affinity. In all cases, some streptavidin molecules might bind only physically, which is termed unspecific binding and is undesirable.

First the surface of the GNP sample must be modified by a mixture of a hydroxyl terminated thiol (Fig. 9.9b) and a biotinilated thiol (Fig. 9.9c). Because of the geometrical structure of the streptavidin molecule, it is necessary to offer biotin on a spacer above the surface and to dilute the biotin on the surface to avoid steric hindrance during the binding process. The dilution is achieved by hydroxyl terminated thiol [38]. Samples were immersed in a mixture of 0.45 M hydroxyl terminated thiol ethanol solution and 0.05 M biotinilated thiol for self assembly for 45 min. Washing with copious amounts of ethanol

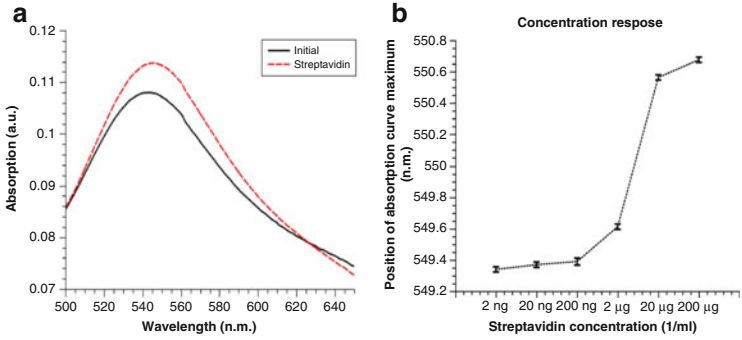

Fig. 9.10 (**a**) Absorption spectra of before and after streptavidin binding, (**b**) streptavidin concentration versus the wavelength position of the absorption maximum

removes the unbounded compounds from the surface. Biotin-modified samples were immersed in various concentrations of streptavidin solution in PBS buffer. After each immersion samples were rinsed with buffer solution. Streptavidin binding causes a red shift in the absorption spectrum (Fig. 9.10a).

Increasing the concentration causes increasing red shifts until a sensing saturation is reached. Figure 9.10b shows the streptavidin concentration response of the GNP sensor.

9.4 Modeling of Surface-Immobilized GNP Biosensors

The motivation for the theoretical study is to develop GNP biosensors of increasing sensitivity by varying the structure of the GNPs, the geometry of the arrangement, and ambient conditions. The optical response of GNPs is analyzed by calculating the LSPR spectrum in the presence of substrates, analytes, etc. The theoretical problem is the determination of the extinction spectra of an incident electromagnetic field upon interaction with a noble-metal nanoparticle and ambient structures.

For GNPs with diameters greater than 10 nm, we can ignore quantum effects and the problem reduces to the solution of Maxwells equations subject to the boundary conditions of a metal nanoparticle an object smaller than the wavelength of the incident field. The

dielectric function of gold can be modeled by the Drude model or the exact values from data tables can be used. The methods we present include frequency-domain methods such as the Discrete-Dipole Approximation, Generalized Mie theory and GranFilm, and a popular time-domain method: the Finite-Difference Time-Domain (FDTD) approximation method.

Both gold and silver have small absorption losses in the optical regime. The dielectric function of gold has a negative real part and a small imaginary part in the visible range of the spectrum. For most metals, the absorption peak wavelength and width depend both on the real and imaginary part of the dielectric function. However, for noble metals, the LSPR peak wavelength depends only on the real part of the dielectric function and not on the imaginary part. The width of the resonance peak depends only on the imaginary part of the dielectric function and not on the real part [25].

Increasing the index of refraction of the dielectric environment both red-shifts the LSPR peak and increases its width. The change in LSPR peak wavelength with respect to ambient refractive index is proportional to the ratio of $\mathrm{Re}[\varepsilon*]$ and the slope of $\mathrm{Re}[\varepsilon*]$ at the plasmon wavelength [30]. For well-separated NPs, there is linear relation between the peak wavelength and the ambient refractive index.

When two or more nanoparticles are in proximity to each other, interactions between the induced multipoles within each particle become increasingly important. The LSPR peaks differ for a single nanoparticle and those having multiple neighbors, which exhibit collective dipole resonances. There are two types of electromagnetic interactions that take place between the nanostructures: near-field coupling and far-field dipolar interactions. When the elements are placed $d<\lambda$ apart, static dipolar interactions dominates with $1/d^3$ dependence on nanoparticle separation. For elements that are placed at a distance $d\simeq\lambda$ in the far-field, radiative dipolar coupling dominates with a $1/d$ dependence on nanoparticle separation. In this chapter, we only examine near-field coupling.

The polarization of the incident light that cause the induced multipoles also becomes important. Consider two spherical particles and the incident light propagating perpendicular to the interparticle axis. The peak shift when the electric field vector is parallel to the interparticle axis (i.e., longitudinal or s-polarized) is different from the peak shift when the electric field vector is perpendicular to the interparticle axis (i.e., transverse or p-polarized). An explanation for this effect is provided in [32, 35]. When the electric field vector is parallel to the

interparticle axis (i.e., longitudinal or s-polarized), the induced local field between the two particles is in the same direction as the applied field as seen in Fig. 1.4a of [35]. The Coulomb forces subtract giving rise to red-shifted LSPR peaks. For cases where the electric vector is perpendicular to the interparticle axis (i.e., transverse or p-polarized), the induced local field between the two particles is in the opposite direction as the applied field as seen in Fig. 1.4b of [35]. The near-field electromagnetic fields interact with a nonbonding type of interaction, and the Coulomb forces add resulting in blue-shifted LSPR peaks. Calculations by Rooney et al. have shown that the effect of interparticle proximity can be achieved by coating with a dielectric material, an effect called optical clustering [36].

In the results presented, we give the extinction spectra of the various nanoparticle configurations. The extinction cross-section describes the effect of the interaction of the scattered field and particle with the incident field. Assume an incident beam of radiation is incident upon on isolated particle. The rate at which energy is lost due to the presence of the particle as the sum of the energy absorbed and scattered $W_{ext} = W_a + W_s$. The cross-sections will be defined as the fraction of the rate of energy deposition to the incident irradiance, I_i:

$$C_{ext} = \frac{W_{ext}}{I_i},$$

which will have dimensions of area. Similar expressions exist for C_a and C_s and accordingly $C_{ext} = C_a + C_s$. To avoid the note keeping of units we will work in terms of the efficiency factors defined to be unitless according to:

$$Q_{ext} = \frac{C_{ext}}{A},$$

where A is the cross-sectional area of the particle.

9.4.1 Macroscopic Theories

For a single spheroidal nanoparticle with dimension much smaller than wavelength of light, the absorption spectrum can be calculated to experimental accuracy using the well-known Mie theory [7, 29]. The Mie scattering method calculates the optical properties of single spherical particles of any radius using classical electrodynamics.

The incident light sets up the localized surface plasmon oscillation, and the induced potential is to a good approximation, a dipole. The spectrum of the reradiated light is calculated, and this has a peak whose wavelength depends on factors such as the nanostructure's size, shape, dielectric properties of the material, surrounding environment, and the incident field's polarization [47]. This analytical method provides an exact solution to Maxwell's equations for an electromagnetic wave scattered from a spherical particle, and is therefore used to benchmark numerical and approximation methods.

There are several approximate analytic methods for modeling point dipoles and their interactions. Some of them are: the electrostatic approximation method replaces Maxwell's equations with LaPlace equations and is valid for particles smaller than 10 nm [18]. The modified long-wavelength approximation is a perturbative correction of the electrostatic treatment and is relatively accurate for particles that are as large as 10% of the wavelength of the driving field. In the single-dipole approximation (SDA) method, each particle is treated as a single dipole scatterer [11]. The SDA method is accurate for small (dimension << wavelength) and well-separated spherical particles. The coupled dipole approximation (CDA) is a method to include interparticle interactions. Each particle is treated as a single dipole, and two particles interact via dipole–dipole interactions [17]. All these methods work best for very small particles that are fairly well separated.

Other methods involve homogenization and these are sometimes called effective medium theories. Examples are Maxwell–Garnett [28] and the Marton–Schlesinger [27] methods. These well-known methods homogenize the solutions to the Maxwell equations in the presence of three-dimensional inhomogeneous media. Recently, Cheng, Rangan, and Sipe have developed an analytic theory for the homogenization of Maxwell's equations in media that are inhomogeneous only along two dimensions [9]. These methods also make the assumption that the nanoparticles are effectively point dipoles, although some corrections for finite size can be made.

To model the experimental situation of interest, OMCVD deposited nanoparticles on a substrate, a more accurate method is found to be required. We examine four methods: the Discrete Dipole Approximation (DDA), the Bedeaux–Vlieger method (GranFilm), the Generalized Multiparticle Mie (GMM), and FDTD in order to model this experimental geometry. In all methods, we use the dielectric

function of gold from data tables. All three methods are benchmarked against Mie theory for a single spherical GNP of radius 20 nm.

9.4.2 GMM Theory

The extrapolation of Mie Theory to the multiparticle system is referred to as generalized multiparticle (sometimes referred to as multipole) Mie Theory, or GMM. While several variations of the theory currently exist, we use and evaluate the approach of Xu [46]. In this method, "partial scattering coefficients" account for the scattering of particle *i* due to the field from particle *j*.

The number of terms used in the harmonic expansions of the scattering coefficients is determined by Wiscombe's criterion [43] which poses an a priori method of estimating the number of terms to sufficiently model the system. The criterion relates the number of terms N to the size parameter of a single particle, $x = \pi a / \lambda$ where a is the radius of the particle and λ is the wavelength of incident radiation. It states that:

$$N = \begin{cases} x + 4x^{1/3} + 1 & 0.02 \le x \le 8 \\ x + 4.05x^{1/3} + 2 & 8 < x < 4{,}200 \\ x + 4x^{1/3} + 2 & 4{,}200 \le x \le 20{,}000 \end{cases} \tag{9.1}$$

For the calculations presented here, spectral convergence was achieved with $N=7$.

9.4.3 Discrete Dipole Approximation

One numerical method that is suitable for the study of small clusters ($N = 2-10$) of nanoparticles (10 – 30 nm) is the well-known DDA. Developed by Draine and Flatau [12, 13] for modeling atmospheric phenomena, the DDA relies on the approximation of a continuous material by a discretized cubic grid of N point dipoles. One of the limitations of the method is the faithful representation of target surfaces. This problem could be circumvented by increasing dipole density in high-curvature surface regions, but this means giving up the use of the Fast Fourier transform algorithm that requires

equally spaced grid points. We are interested in the extinction cross-section of the particles, or the sum of the absorption and scattering cross-sections.

The validity criterion for the DDA is the long-wavelength approximation: $|m|kd<1$ where m is the complex refractive index, k is the wave number and d the grid spacing. We choose the grid spacing to be small enough so as to satisfy this criterion.

A second advantage of this method is that we can plot contour maps of the evanescent field around a metal nanoparticle. This gives us the ability to extract optoelectrical information at an extremely small surface. A limitation of this method is that computational resources (memory and time) place a limit on the size of the nanoparticles and/or the number of particles in a cluster.

9.4.4 Optical Properties of Nanoparticles on a Surface

The Bedeaux–Vlieger [5] method is a homogenization method that has provided quantitative calculations of the optical properties of nanoparticles on a surface. The GranFilm program developed by Lazzari and Simonsen [22] is designed to investigate the optical properties of granular thin films. The island polarizabilities are computed by solving the LaPlace equation in the quasi-static limit. This is accomplished through a multipole expansion with the presence of the surface taken into account through the method of images. The island polarizabilities are determined as the first order coefficients in the expansion. The presence of and interaction between islands are treated through a modification of the polarizability.

This method accounts for the multipolar coupling interaction between particle and substrate through the fulfillment of the boundary conditions, and the coupling effects between particles up to quadrupolar order. The advantage of this method is that single-particle-substrate interactions can be treated easily and accurately. The disadvantage is that for closely spaced particles the present implementation does not accurately account for higher multipolar interactions. Another limitation of these methods is that the electric field itself cannot be mapped, and more complex structures (such as nanoparticles made of concentric shells of materials) cannot be modeled. Note that later modifications of this method [23] have made it possible to

visualize the multipolar potential yielding more physical insights into this problem.

A nice feature of GranFilm is that in addition to the square lattice arrangement (with a lattice constant input), the GranFilm program also has the capability to model random arrangements of particles through a mean field theory approximation. In the latter case, fraction of coverage is determined according to:

$$C = \frac{4\pi r^2}{(4r+d)^2}, \tag{9.2}$$

where r denotes the particle radius and d the mean interparticle spacing.

9.4.5 The FDTD Method

The FDTD method is a time-domain numerical approach to model light-matter interactions based on electrodynamics calculations [39]. Maxwell's equations are solved by discretizing them with central-difference approximations that are accurate to the second-order for both space and time derivatives. The resulting finite-difference equations are solved numerically. By using Fourier transforms, the FDTD method can also be used to calculate quantities as a function of frequency such as normalized transmission and far-field projection. The FDTD software package used in this study is developed by Lumerical Solutions™. Electrodynamics calculations are solved based on Yee-cell mesh grids and a leap-frog update approach [45].

Since the E- and H-fields are computed at all points within the simulation volume at each time step, animated displays of the system's time-dependent electromagnetic response can be created. This technique is particularly valuable for applications that require a broad range of wavelengths for analysis such as interactions with short pulses. Some other advantages include the possibility of simulating infinitely long chains/arrays of nanoparticles (using periodic boundary conditions), producing contour plot visualizations of the electric and magnetic fields, integrating scripts compatible with Matlab, and running parallel computation for more sophisticated post processing techniques.

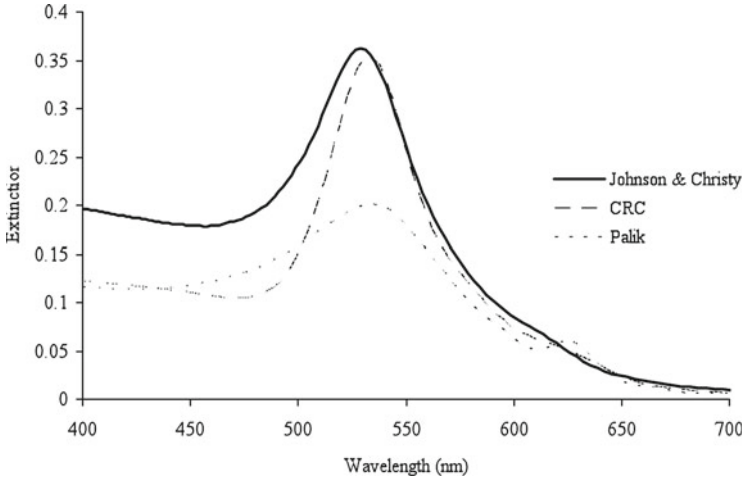

Fig. 9.11 Spectra of spherical gold nanoparticle of radius 20 nm calculated using optical constants from different data tables

A known issue of FDTD methods is that the decrease in the mesh size leads to convergence of the peak wavelength, but not of the spectrum itself. Thus, the peak wavelength of the LSPR wavelength was monitored for convergence testing. The FDTD method was calibrated by performing convergence tests for different Au particle sizes. It was found that the FDTD method yields accurate LSPR spectral peak values for particles with radius greater than 20 nm as compared with Mie theory.

9.4.6 Sensitivity to Gold Dielectric Constant Data

An unexpected finding of the FDTD calculations was the sensitivity of the spectra to the gold dielectric constant data input. Optical constants for gold were obtained from Palik [34], CRC optical data tables [33], and Johnson & Christy's optical tables [19]. Converged spectra using all three input data show LSPR peak positions at 529 nm, 533 nm, and 533 nm for Johnson & Christy, CRC, and Palik, respectively (see Fig. 9.11). The extinction represents the summation of absorption and scattering where the percentage of power transmitted is recorded by the field monitors.

We also note that the Lumerical's implementation of the FDTD program fits the input optical constant data to a polynomial, and all three programs are fit by quite different polynomials as seen in Fig. 9.12.

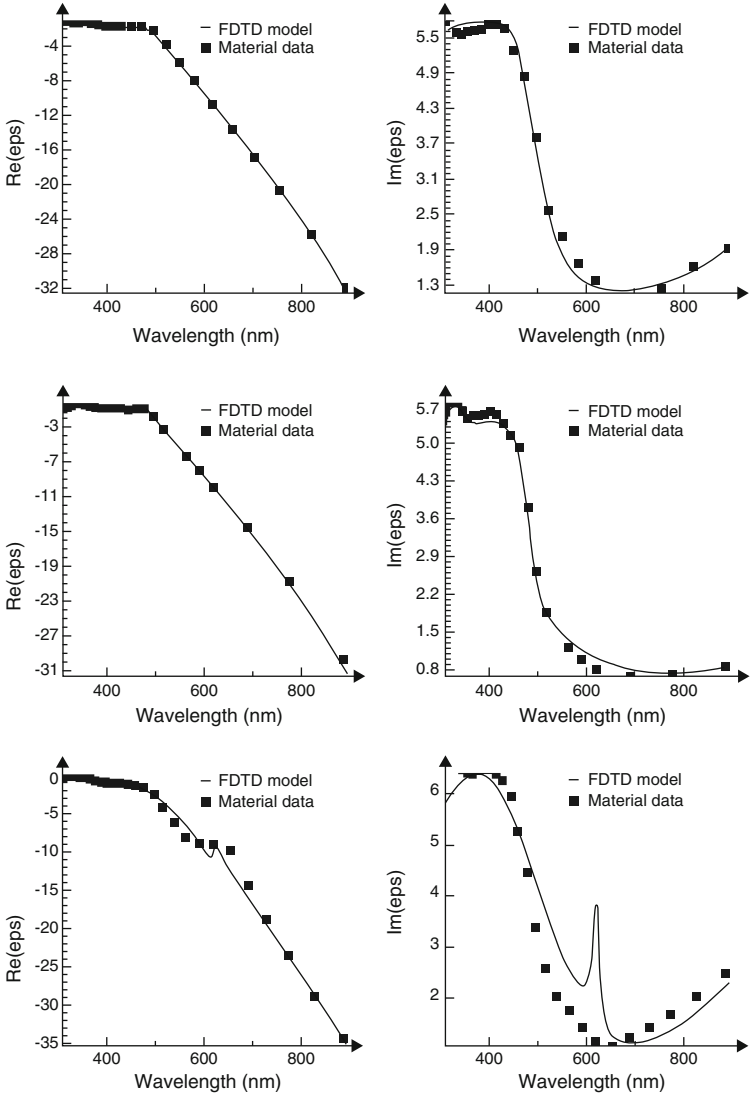

Fig. 9.12 The optical constants of gold from various data tables and their polynomial fits provided by the FDTD program. Johnson & Christy (*top*), CRC (*middle*), and Palik (*bottom*)

9.5 Comparison Between Experimental Samples and Theoretical Models

9.5.1 OMCVD Experiments

The OMCVD experiment data were measured using UV-VIS spectroscopy at the University of Western Ontario by Dr. Silvia Mittler and Erden Ertorer. The data samples, referred to as L3, L6, L9, M9, M10, and M11, were constructed with the purpose of random sizes and spacings. After production, the particle sizes and spacings were measured and were received via several histograms as shown in Fig. 9.7. The data samples L3, L6, and L9 were bare nanoparticles on a glass substrate. The samples M9, M10, and M11 contained surface-immobilized nanoparticles that were coated with organic material of hydrodynamic radius of 1 nm.

To model the particle distributions, the system was modeled through the use of two GNPs separated by a finite center-to-center distance d. The size and spacings of the particles were varied and weighted according to the experimentally provided data. The coating of organic material on the nanoparticles in samples "M" were modeled by a concentric coating of thickness 1 nm and refractive index 1.35. The particles were subjected to two perpendicular polarizations directed parallel to and perpendicularly to the interparticle axis. We also calculated the spectra for unpolarized incident light.

For the above calculations, the radii of the nanoparticles were assumed to be identical and were varied, along with the interparticle spacing (center-to-center distance). To compare with experiments, the weighted averages of the spectra were calculated according to the following approximations.

First, we calculated the spectrum of two nanoparticles of the average radius, and separated by the average interparticle separation (these are labeled by "Avg.")

$$Q_{\text{ext,avg}} = q. \tag{9.3}$$

where q will be used to simplify the notation for the calculated extinction value. Next, we assumed that the spread in the particle radii could be neglected and therefore we took the particles to be of the average radius, but weighted the spectra according to the interparticle spacing histogram (labeled Ravgov)

$$Q_{\text{ext,Ravg}} = \frac{1}{\sum_j w_j} \sum_j w_j q_j, \tag{9.4}$$

where summation is taken over all experimentally measured spacings [4 nm – 64 nm in 4 nm increments] and *wj* is the fraction of experimentally observed particles with spacing j. Since overlapping particles might be considered as larger particles, we calculated the same quantity as above, but omitting the overlapping particles in the weighting (Ravgno). The final level of approximation was to weight the spacings and radii according to the experimental histograms (labeled by "Allov"). For the same reason as above, we repeated the calculation without the overlapping particles (labeled by "Allno").

$$Q_{\text{ext,all}} = \frac{1}{\sum_{i,j} w_i w_j} \sum_{i,j} w_i w_j q_i q_j \tag{9.5}$$

where the first summation is taken over all experimentally observed particle radii (2 nm – 20 nm in 2 nm increments), and the second is taken over all possible spacings as done previously.

These approximations were run for the DDA, GMM, and GranFilm methods with the exceptions that GMM and GranFilm cannot study overlapping particles as their fundamental theories break down [2, 21].

All results were then scaled to experimental measurements according to

$$s = \left| \frac{Q_{\text{exp},N} - Q_{\text{exp,max}}}{Q_{\text{theory},N} - Q_{\text{theory,max}}} \right| \tag{9.6}$$

$$Q_{\text{ext,scaled}} = sQ_{\text{theory}} + \left(Q_{\text{exp,max}} - sQ_{\text{theory,max}}\right) \tag{9.7}$$

where N is the number of frequencies used in the compution, i.e. $Q_{ext,N}$ is the final extinction value in the calculated spectrum.

9.5.2 Results of the Comparison

For all three methods, the third weighting approximation $Q_{\text{ext,all}}$ allowing for overlapping particles where possible produced the best agreement with experiment. Plots of experimentally measured and selected calculated spectra are shown in Figs. 9.13–9.30.

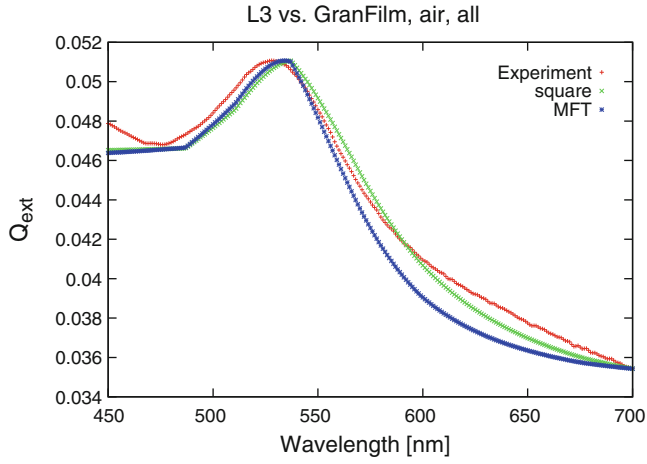

Fig. 9.13 Sample L3: OMCVD deposited GNPs. Comparison between experimental spectra and spectra calculated using GranFilm. In the calculations, the "Allno" averaging was employed for both square lattice GNP arrangements ("square") and random arrangements using mean field theory ("MFT")

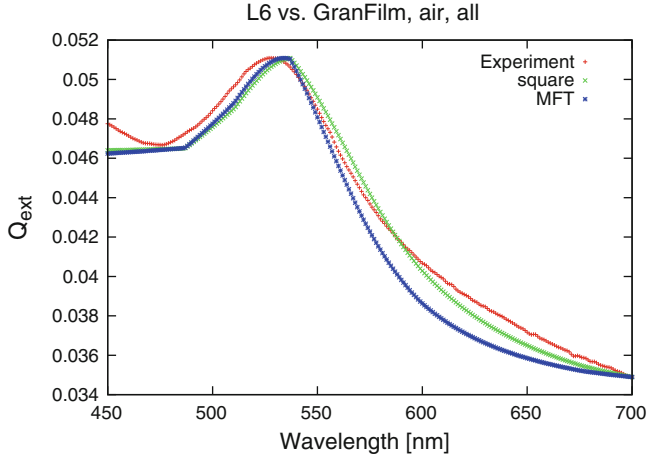

Fig. 9.14 Sample L6: OMCVD deposited GNPs. Comparison between experimental spectra and spectra calculated using GranFilm. In the calculations, the "Allno" averaging was employed for both square lattice GNP arrangements ("square") and random arrangements using mean field theory ("MFT")

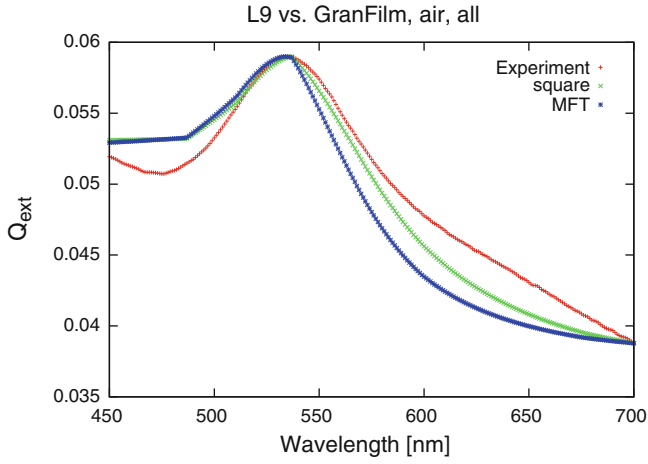

Fig. 9.15 Sample L9: OMCVD deposited GNPs. Comparison between experimental spectra and spectra calculated using GranFilm. In the calculations, the "Allno" averaging was employed for both square lattice GNP arrangements ("square") and random arrangements using mean field theory ("MFT")

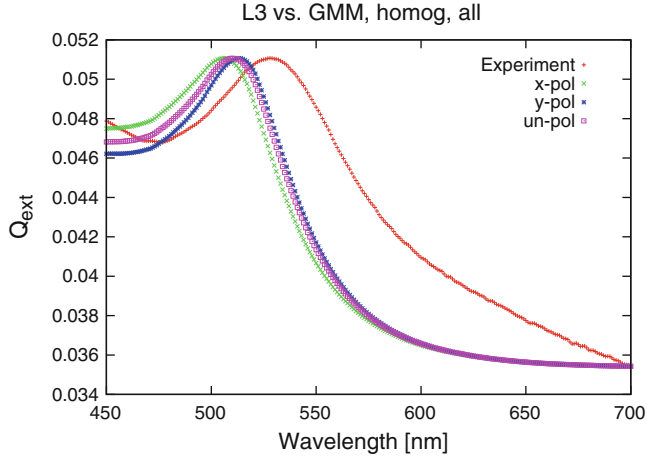

Fig. 9.16 Sample L3: OMCVD deposited GNPs. Comparison between experimental spectra and spectra calculated using the GMM method. In the calculations, the "Allno" averaging was employed for s-polarized ("x"), p-polarized ("y"), and unpolarized ("un-pol") incident light

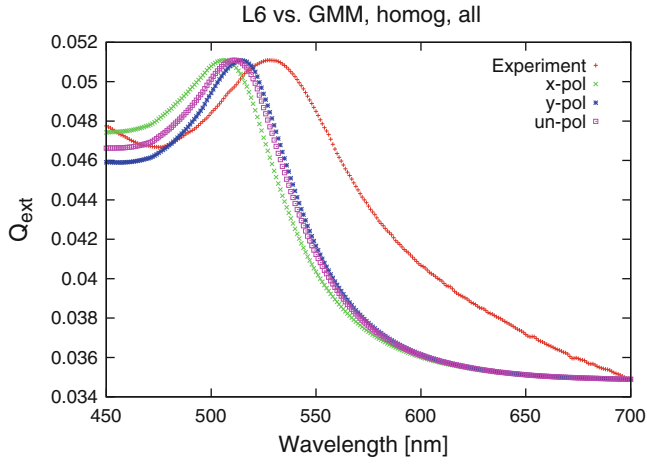

Fig. 9.17 Sample L6: OMCVD deposited GNPs. Comparison between experimental spectra and spectra calculated using the GMM method. In the calculations, the "Allno" averaging was employed for s-polarized ("x"), p-polarized ("y"), and unpolarized ("un-pol") incident light

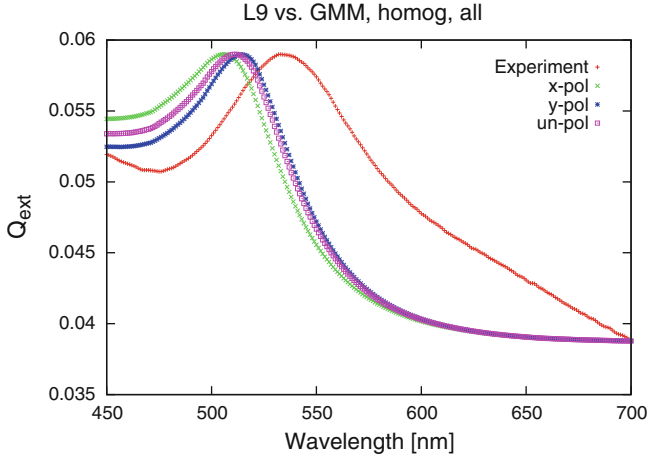

Fig. 9.18 Sample L9: OMCVD deposited GNPs. Comparison between experimental spectra and spectra calculated using the GMM method. In the calculations, the "Allno" averaging was employed for s-polarized ("x"), p-polarized ("y"), and unpolarized ("un-pol") incident light

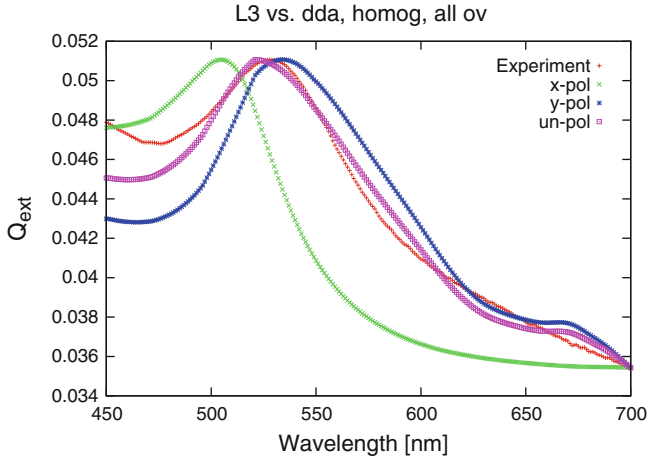

Fig. 9.19 Sample L3: OMCVD deposited GNPs. Comparison between experimental spectra and spectra calculated using the DDA method. In the calculations, the "Allov" averaging was employed for s-polarized ("x"), p-polarized ("y"), and unpolarized ("un-pol") incident light

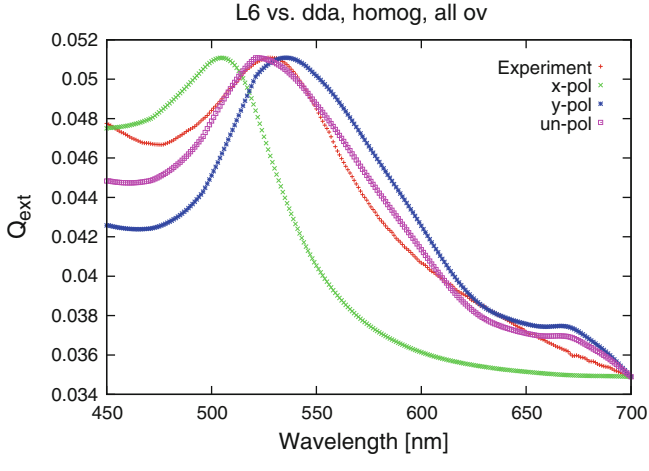

Fig. 9.20 Sample L6: OMCVD deposited GNPs. Comparison between experimental spectra and spectra calculated using the DDA method. In the calculations, the "Allov" averaging was employed for s-polarized ("x"), p-polarized ("y"), and unpolarized ("un-pol") incident light

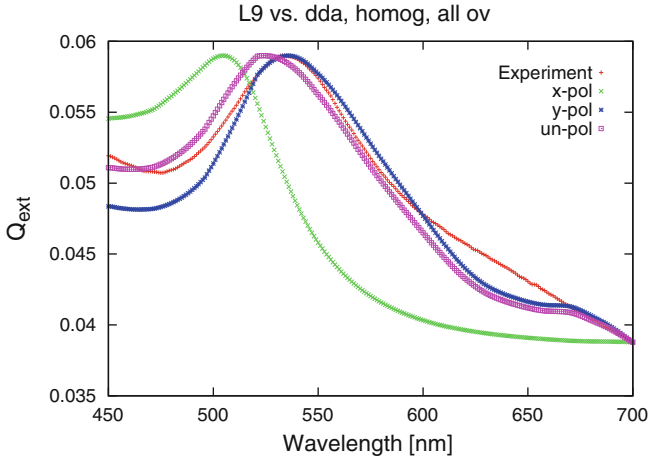

Fig. 9.21 Sample L9: OMCVD deposited GNPs. Comparison between experimental spectra and spectra calculated using the DDA method. In the calculations, the "Allov" averaging was employed for s-polarized ("x"), p-polarized ("y"), and unpolarized ("un-pol") incident light

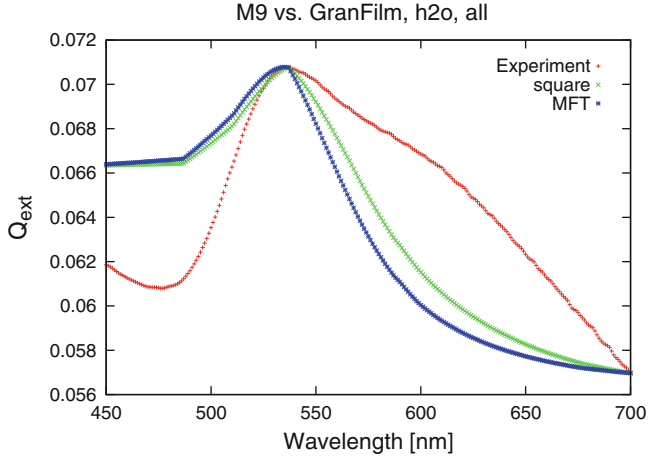

Fig. 9.22 Sample M9: OMCVD deposited GNPs [coated with a layer of ethanol]. Comparison between experimental spectra and spectra calculated using GranFilm. In the calculations, the "Allno" averaging was employed for both square lattice GNP arrangements ("square") and random arrangements using mean field theory ("MFT")

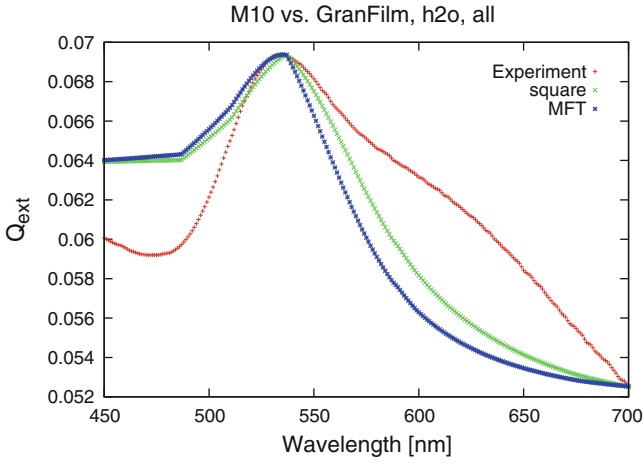

Fig. 9.23 Sample M10: OMCVD deposited GNPs [coated with a layer of ethanol]. Comparison between experimental spectra and spectra calculated using GranFilm. In the calculations, the "Allno" averaging was employed for both square lattice GNP arrangements ("square") and random arrangements using mean field theory ("MFT")

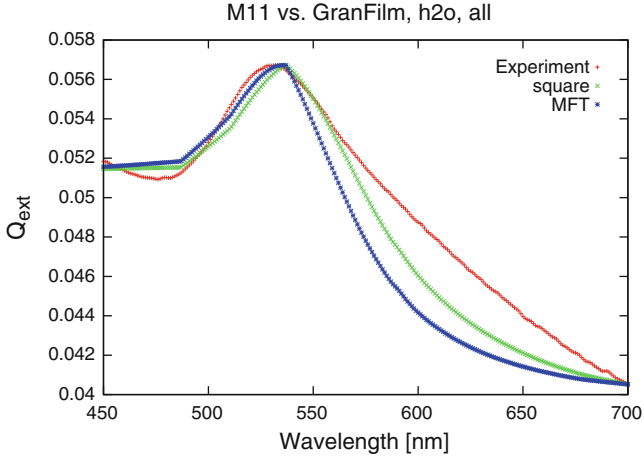

Fig. 9.24 Sample M11: OMCVD deposited GNPs [coated with a layer of ethanol]. Comparison between experimental spectra and spectra calculated using GranFilm. In the calculations, the "Allno" averaging was employed for both square lattice GNP arrangements ("square") and random arrangements using mean field theory ("MFT")

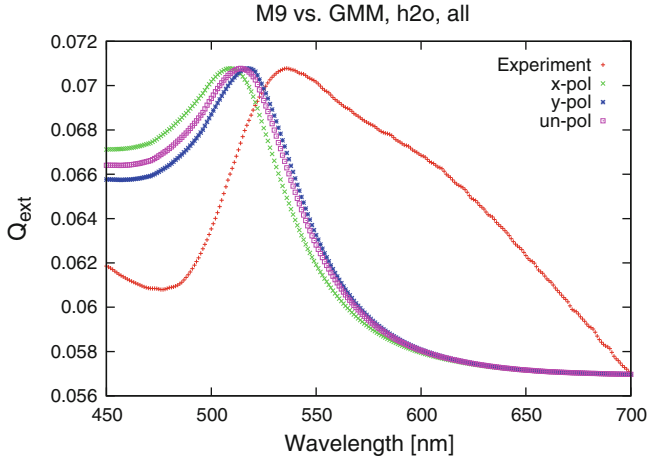

Fig. 9.25 Sample M9: OMCVD deposited GNPs [coated with a layer of ethanol]. Comparison between experimental spectra and spectra calculated using the GMM method. In the calculations, the "Allno" averaging was employed for s-polarized ("x"), p-polarized ("y"), and unpolarized ("un-pol") incident light

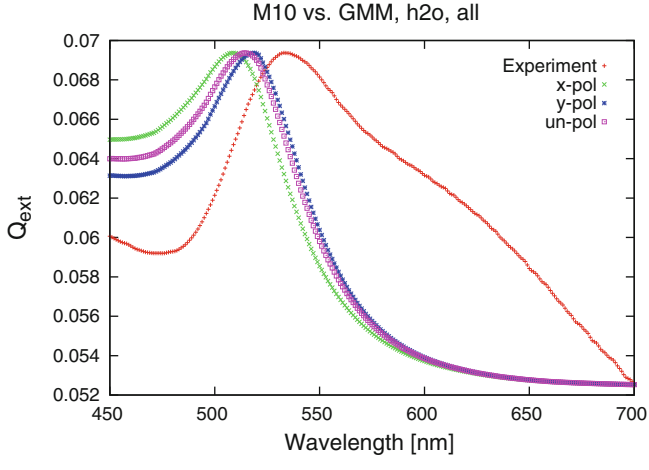

Fig. 9.26 Sample M10: OMCVD deposited GNPs [coated with a layer of ethanol]. Comparison between experimental spectra and spectra calculated using the GMM method. In the calculations, the "Allno" averaging was employed for s-polarized ("x"), p-polarized ("y"), and unpolarized ("un-pol") incident light

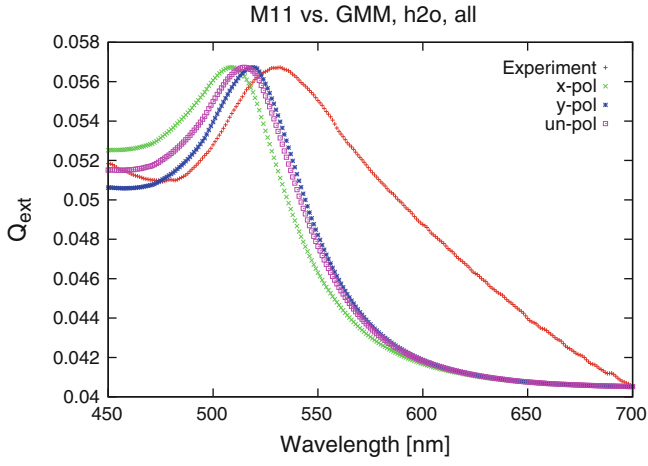

Fig. 9.27 Sample M11: OMCVD deposited GNPs [coated with a layer of ethanol]. Comparison between experimental spectra and spectra calculated using the GMM method. In the calculations, the "Allno" averaging was employed for s-polarized ("x"), p-polarized ("y"), and unpolarized ("un-pol") incident light

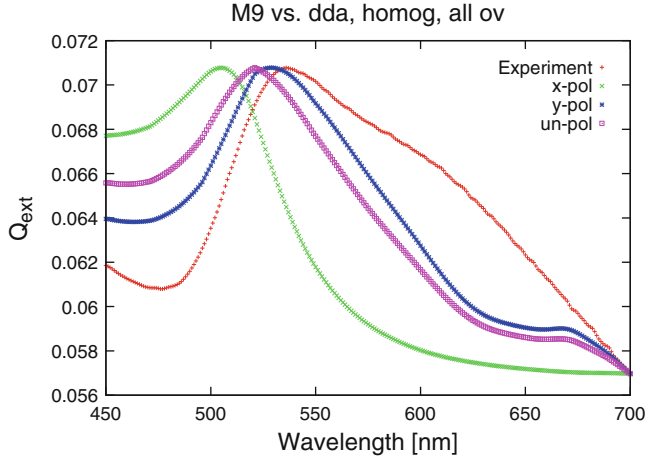

Fig. 9.28 Sample M9: OMCVD deposited GNPs [coated with a layer of ethanol]. Comparison between experimental spectra and spectra calculated using the DDA method. In the calculations, the "Allov" averaging was employed for s-polarized ("x"), p-polarized ("y"), and unpolarized ("un-pol") incident light

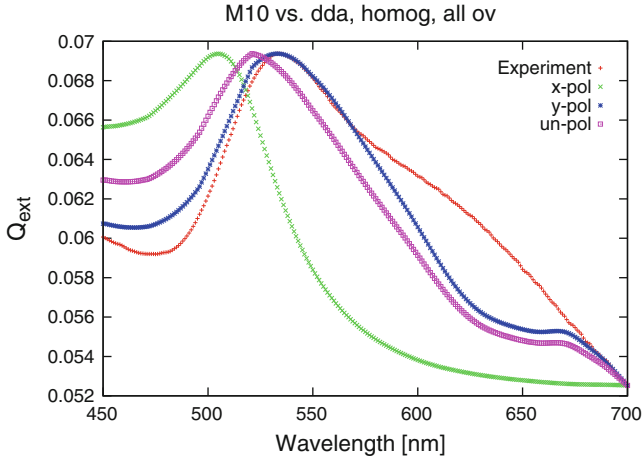

Fig. 9.29 Sample M9: OMCVD deposited GNPs [coated with a layer of ethanol]. Comparison between experimental spectra and spectra calculated using the DDA method. In the calculations, the "Allov" averaging was employed for s-polarized ("x"), p-polarized ("y"), and unpolarized ("un-pol") incident light

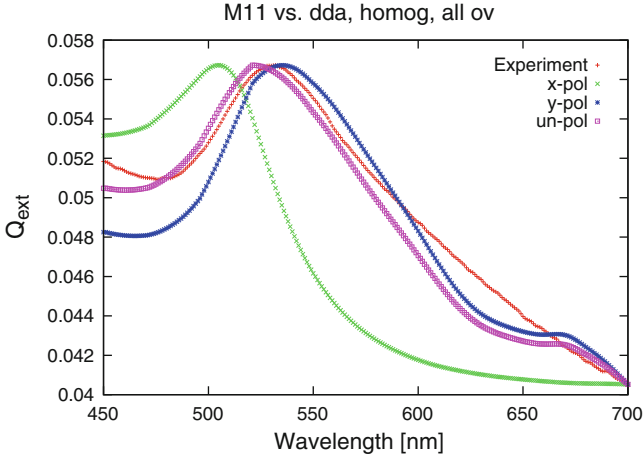

Fig. 9.30 Sample M9: OMCVD deposited GNPs [coated with a layer of ethanol]. Comparison between experimental spectra and spectra calculated using the DDA method. In the calculations, the "Allov" averaging was employed for s-polarized ("x"), p-polarized ("y"), and unpolarized ("un-pol") incident light

9.6 Summary

OMCVD is an easy and inexpensive method to fabricate GNPs on substrate surfaces. Flatness of the reactor bottom, heating method, and the quality of the surface functionalization are crucial for the stability and uniformity of the nanoparticles. Automatization of the processes increases the quality. SEM and UV-Vis absorption spectroscopy are helpful tool to characterize samples and control quality. SEM images were used to yield size and interparticle distance data. UV-Vis absorption spectroscopy can be used as a gauge of uniformity in particle size. Bulk and protein sensing experiments show that OMCVD grown GNPs are suitable for highly sensitive biosensor applications (Figs. 9.8–9.10).

From the modeling perspective, it was found that the DDA method gave the best comparisons with experiments. We find that it is necessary to have a weighted average of size and spacing distributions especially for the coated particles. This confirms the "optical clustering" hypothesis put forth in [35, 36]. The two-particle model works surprisingly well indicating that nearly all the physics is described by the single particle LSPR and the two-particle cross talk. The two particle cross-talk is mediated either by the proximity of the two bare GNP surfaces or by a coating on two not-so-proximate nanoparticles. The FDTD time-domain method showed a surprising sensitivity to input optical constants data. Even though the data from different sources themselves were similar, the fitting program gives completely different polynomial fits, and the best fit was for the data from Johnson and Christy.

A long-time desire of experimentalists is the ability to extract from UV-Vis absorption data of coated nanoparticles on surfaces, the thickness and refractive index of the analyte. This would be another alternative to planar surface plasmon spectroscopy. We are not there yet, but this work demonstrates that we are getting closer to this goal.

Acknowledgements Research support by the Natural Sciences and Engineering Research Council of Canada (Discovery Grants and NSERC Strategic Network on Bioplasmonic Systems) and Canada Foundation for Innovation is gratefully appreciated. Computations were done on the SharcNet (Compute Canada) supercomputing network. Silvia Mittler thanks the Canada Research Chairs program of the Canadian government. Ertorer was partly supported by the Ontario Graduate Scholarship and the Ontario Graduate Scholarship for Science and Technology.

References

1. Abramoff MD, Magalhes PJ, Ram SJ. Image processing with ImageJ. Biophoton Int. 2004;11(7):36–42.
2. Alivisatos AP. Science. 1996;271:933.
3. Aliganga AKA, Duwez AS, Mittler S. Binary mixtures of self-assembled monolayers of 1,8-octanedithiol and 1-octanethiol for a controlled growth of gold nanoparticles. Org Electron. 2006;7(5):337–50.
4. Aliganga AKA, Lieberwirth I, Glasser G, Duwez A-S, Sun Y, Mittler S. Fabrication of equally oriented pancake shaped gold nanoparticles by SAM templated OMCVD and their optical response. Org Electron. 2007;8: 161–74.
5. Bedeaux D, Vlieger J. Optical properties of surfaces. 2nd ed. Singapore: World Scientific; 2004.
6. Bharathi S, Fishelson N, Lev O. Direct synthesis and characterization of gold and other noble metal nanodispersions in sol-gel-derived organically modified silicates. Langmuir. 1999;15(6):1929–37.
7. Bohren CF, Huffman DR. Absorption and scattering of light by small particles. New York: Wiley Interscience; 1983.
8. Chen C-D, Cheng S-F, Chau L-K, Wang CRC. Sensing capability of the localized surface plasmon resonance of gold nanorods. Biosensors Bioelectron. 2007;22:926–32.
9. Cheng T, Rangan C, Sipe JE. Metallic nanoparticles on waveguide structures: effects on waveguide mode properties, and the promise of sensing applications (manuscript); Journal of the Optical Society of America B (in press).
10. Daniel M, Astruc D. Gold nanoparticles: assembly, supramolecular chemistry, quantum-size-related properties, and applications toward biology, catalysis, and nanotechnology. Chem Rev. 2004;104:293–346.
11. Doyle WT. Optical properties of a suspension of metal spheres. Phys Rev B. 1989;39(14):9852–8.
12. Draine BT, Flatau PJ. J Opt Soc Am A. 1973;11:1491.
13. Draine BT, Goodman JJ. ApJ. 1993;485:685.
14. Fischer RA, Weckenmann U, Winter C, Kshammer J, Scheumann V, Mittler S. Area selective OMCVD of gold and palladium on self-assembled organic monolayers: control of nucleation sites. J Phys IV France. 2001;11(PR3):Pr3-1183–Pr3-1190.
15. Frederix F, Bonroy K, Laureyn W, Reekmans G, Campitelli A, Dehaen W, Maes G. Enhanced performance of an affinity biosensor interface based on mixed self-assembled monolayers of thiols on gold. Langmuir. 2003;19(10): 4351–7.
16. Hampden-Smith MJ, Kodas TT. Chemical vapor deposition of metals: Part 1. An overview of CVD processes. Chem Vapor Deposition. 1995;1(1):8–23.
17. Haynes CL, McFarland AD, Zhao L, Van Duyne RP, Schatz GC. Nanoparticle optics: the importance of radiative dipole coupling in two-dimensional nanoparticle arrays. J Phys Chem B. 2003;107:7337–42.
18. Jensen T, Kelly L, Lazarides A, Schatz GC. Electrodynamics of noble metal nanoparticles and nanoparticle clusters. J Cluster Sci. 1999;10:295–317.

19. Johnson PB, Christy RW. Optical constants of the noble metals. Phys Rev B. 1972;6:4370–9.
20. Käshammer J, Wohlfart P, Wei J, Winter C, Fischer R, Mittler-Neher S. Selective gold deposition via CVD onto self-assembled organic monolayers. Opt Mater. 1998;9:406–10.
21. Kreibig U, Vollmer M. Optical properties of metal clusters. Berlin: Springer; 1995.
22. Lazzari R, Simonsen I. GRANFILM: a software for calculating thin-layer dielectric properties and Fresnel coefficients. Thin Solid Films. 2002;419(1–2):124–36.
23. Lazzari R, Simonsen I, Bedeaux D, Vlieger J, Jupille J. Eur Phys J B. 2001; 24:267.
24. Link S, El-Sayed MA. Size and temperature dependence of the plasmon absorption of colloidal gold nanoparticles. J Phys Chen B. 1999;103: 4212–7.
25. Maier SA. Guiding of electromagnetic energy in subwavelength periodic metal structures. Ph.D. Thesis, California Institute of Technology, Pasadena; 2003.
26. Manifar T, Rezaee A, Sheikhzadeh M, Mittler S. Formation of uniform self-assembly monolayers by choosing the right solvent: OTS on silicon wafer, a case study. Appl Surface Sci. 2008;254(15):4611–9.
27. Marton P, Schlesinger M. J Electrochem Soc. 1968;115:16.
28. Maxwell-Garnett JC. Philos Trans R Soc Lond. 1904;203:385; Ser A 1906;205:237.
29. Mie G. Beitrge zur Optik trber Medien speziell kolloidaler Goldlsungen. Ann Phys. 1908;25:377–445.
30. Miller MM, Lazarides AA. Sensitivity of metal nanoparticle plasmon resonance band position to the dielectric environment as observed in scattering. J Opt A: Pure Appl Opt. 2006;8:239–49.
31. Nicolas S, Dufour-Gergam E, Bosseboeuf A, Bourouina T, Gilles J-P, Grandchamp J-P. Fabrication of a gray-tone mask and pattern transfer in thick photoresists. J Micromech Microeng. 1998;8:95.
32. Noguez C. Surface plasmons on metal nanoparticles: the influence of shape and physical environment. J Phys Chem C. 2007;111:3806–19.
33. Weaver JH, Frederikse HPR. Optical Properties of Metals and Semiconductors, CRC Handbook of Chemistry and Physics, 74th Edition and subsequent printings (CRC Press, Boca Raton, Florida) pp. 12–109, 12–131.
34. Palik E. Handbook of optical constants of solids I–III. San Diego: Academic; 1998.
35. Rafsanjani SMH, Cheng T, Mittler S, Rangan C. Theoretical proposal for a biosensing approach based on a linear array of immobilized gold nanoparticles. J Appl Phys. 2010;107:094303.
36. Rooney P, Xu S, Rezaee A, Manifar T, Hassanzadeh A, Podoprygorina G, Bhmer V, Rangan C, Mittler S. Control of surface plasmon resonances in dielectrically-coated proximate gold nanoparticles immobilized on a substrate. Phys Rev B. 2008;77(23):235446.
37. Schott AG, 2007, Data Sheet N-BK7 [Online] Mainz, Germany: Schott. Available at http://www.schott.com/advanced_optics/english/abbe_datasheets/schott_datasheet_n-bk7.pdf. [Accessed 03 January 2013].

38. Spinke J, Liley M, Schmitt F-J, Guder H-J, Angermaier L, Knoll W. Molecular recognition at self-assembled monolayers: optimization of surface functionalization. J Chem Phys. 1993;99(9):7012–19.
39. Taflove A, Hagness SC. Computational electrodynamics: the finite-difference time-domain method. 2nd ed. Boston: Artech House; 2005.
40. Thoma F, Langbein U, Mittler-Neher S. Waveguide scattering microscopy. Opt Commun. 1997;134:16–20.
41. Ulman A. An introduction to ultrathin organic films: from Langmuir-Blodgett to self-assembly, vol Xxiii. London: Academic; 1991. p. 442.
42. Weisser M, Thoma F, Menges B, Langbein U, Mittler-Neher S. Fluorescence in ion exchanged BK7 glass slab waveguides and its use for scattering free loss measurements. Opt Commun. 1998;153:27–31.
43. Wiscombe WJ. Improved Mie scattering algorithms. Appl Opt. 1980;19(9): 1505–9.
44. Wohlfart P, Wei J, Kshammer J, Winter C, Scheumann V, Fischer R, Mittler-Neher S. Selective ultrathin gold deposition by organometallic chemical vapor deposition onto organic self-assembled monolayers (SAMs). Thin Solid Films. 1999;340:274–9.
45. Yee K. Numerical solution of initial boundary value problems involving Maxwell's equations in isotropic media. IEEE Trans Antenn Propag. 1966;14: 302–7.
46. Yu-lin Xu. Electromagnetic scattering by an aggregate of spheres. Appl Opt. 1995;34(21):4573–88.
47. Zou S, Janel N, Schatz GC. Silver nanoparticles array structures that produce remarkably narrow plasmon lineshapes. J Chem Phys. 2004;120(23): 10871–5.